LANGMUIR

pubs.acs.org/Langmuir Article

Acoustic Droplet Vaporization of Perfluorohexane Emulsions Induced by Heterogeneous Nucleation at an Ultrasonic Frequency of 1.1 MHz

R. Ramesh, C. Thimonier, S. Desgranges, V. Faugeras, F. Coulouvrat, J. Laurent, G. Marrelec, C. Contino-Pépin, W. Urbach, C. Tribet, and N. Taulier*

Cite This: *Langmuir* 2023, 39, 15716−15729 Read Online

ACCESS | Metrics & More | Article Recommendations | Supporting Information

ABSTRACT: Droplets made of liquid perfluorocarbon undergo a phase transition and transform into microbubbles when triggered by ultrasound of intensity beyond a critical threshold; this mechanism is called acoustic droplet vaporization (ADV). It has been shown that if the intensity of the signal coming from high ultrasonic harmonics are sufficiently high, superharmonic focusing is the mechanism leading to ADV for large droplets (>3 μm) and high frequencies (>1.5 MHz). In such a scenario, ADV is initiated due to a nucleus occurring at a specific location inside the droplet volume. But the question on what induces ADV in the case of nanometer-sized droplets and/or at low ultrasonic frequencies (<1.5 MHz) still remains. We investigated ADV of perfluorohexane (PFH) nano- and microdroplets at a frequency of 1.1 MHz and at conditions where there is no superharmonic focusing. Three types of droplets produced by microfluidics were studied: plain PFH droplets, PFH droplets containing many nanometer-sized water droplets, and droplets made of a PFH corona encapsulating a single micron-sized water droplet. The probability to observe a vaporization event was measured as a function of acoustic pressure. As our experiments were performed on droplet suspensions containing a population of monodisperse droplets, we developed a statistical model to extrapolate, from our experimental curves, the ADV pressure thresholds in the case where only one droplet would be insonified. We observed that the value of ADV pressure threshold decreases as the radius of a plain PFH droplet increases. This value was further reduced when a PFH droplet encapsulates a micron-sized water droplet, while the encapsulation of many nanometer-sized water droplets did not modify the threshold. These results cannot be explained by a model of homogeneous nucleation. However, we developed a heterogeneous nucleation model, where the nucleus appears at the surface in contact with PFH, that successfully predicts our experimental ADV results.

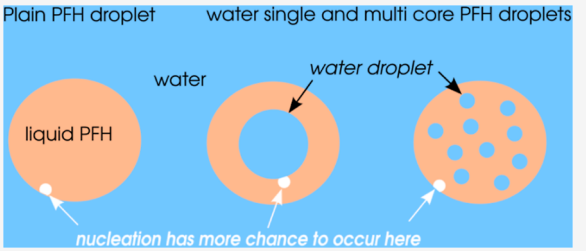

INTRODUCTION

Liquid perfluorocarbons possess a phase change ability; subjecting perfluorocarbon droplets to sufficient acoustic pressure triggers a liquid-to-vapor transition called acoustic droplet vaporization (ADV).[1] The therapeutic potentials of ADV have been exploited for various applications including embolotherapy,[2] phase aberration correction,[3,4] and high-intensity focused ultrasound (HIFU) therapy.[5−9] However, the physics underlying ADV is complex, and the understanding of the ADV mechanism is currently an active research domain. It is admitted that ADV is the result of the appearance of a vapor nucleus, during the rarefactional phase of an acoustic pulse, and of its subsequent growth. Literature investigations have reported that the threshold is a function of the driving ultrasound frequency and pressure, with decreasing pressures needed at higher frequencies.[5,10−12] In addition, droplet size also plays a role, with lower pressures being required for larger droplets.[5,12−14] There is no concrete model capable of predicting all these behaviors. However, a model developed by Shpak et al.[15] is able to predict the location of the initial vaporization nucleus appearance when high ultrasonic harmonics are present with high enough intensity. Indeed, the focusing of these harmonics at a region inside the droplet volume induces a high negative pressure that in turn creates the nucleus whose growth leads to ADV. This effect is all the more efficient when the droplet is large as it requires lower ultrasonic harmonics. Similar observations reported in related studies[16−18] have confirmed the validity of this model. However, this effect is not systematically observed for micron-sized droplets as Shpak et al.[15] determined a nucleation map constructed from ultrahigh-speed imaging, displaying bubbles with nucleation spots located at random positions

Received: August 8, 2023
Revised: October 12, 2023
Accepted: October 13, 2023
Published: October 27, 2023

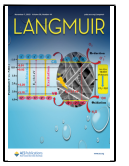

throughout the droplet when its radius was $R = 5.6 \pm 2.1$ μm. According to this model, superharmonic focusing effect is not expected at a low frequency ($f < 1.5$ MHz) or for a small droplet ($R < 3$ μm).[15] Consequently, outside the range of application of the superharmonic focusing effect, another nucleation mechanism is responsible for ADV, in particular for nanometer-sized droplets, which are often used in ADV studies involving medical applications. The search for a mechanism is of course hindered by the fact that individual nanodroplets cannot be detected optically, thus preventing obtaining evidence from direct observations. However, two mechanisms can be expected: homogeneous and heterogeneous nucleations. The appearance of a nucleus of a critical size is responsible for ADV in both these mechanisms. In the first case (i.e., homogeneous nucleation), the nucleus appears inside the droplet volume, while in the second case (i.e., heterogeneous nucleation), it appears at the droplet surface. Current nucleation models show that heterogeneous nucleation can require lesser energy than that needed for homogeneous nucleation.[19] Thus, in some conditions, a nucleus is most likely to appear at the droplet surface than in its volume. Several investigations have already showed the importance of the surface properties in vaporization, suggesting that heterogeneous nucleation takes place in their system.[20,21]

In order to gain a better knowledge of the mechanism that initiates ADV in the absence of superharmonic focusing, we have investigated three types of PFC droplets, which allow us to vary the area and curvature of the surfaces in contact with perfluorocarbon:

1. plain perfluorohexane (PFH) droplets surrounded by a monolayer of a homemade fluorinated surfactant,
2. water multicore PFH droplets, similar to (1) but containing in their core nanodroplets of water surrounded by a shell made of a commercial surfactant, ensuring their dispersion in the PFH, and
3. a water single-core PFH droplet, similar to (2) but with a single water microdroplet instead of several water nanodroplets.

For these three types of emulsions, we have determined, at an ultrasonic frequency of 1.1 MHz, the variation of ADV pressure threshold with the droplet number and size, as well as with the volume fraction of water trapped in the PFH.

MATERIALS AND METHODS

Materials. Unless otherwise stated, all chemicals were used without further purification, and all solutions were filtered using Acrodisc Syringe Filters (from PALL) with a pore size of 0.2 μm. All aqueous solutions were made using Milli-Q IQ 7000 Type-1 water Purification System. Methanol and NaCl were obtained from Sigma-Aldrich. PDMS Sylgard 184 was purchased from Neyco. Photoresist SU8 was purchased from Chimie Tech Services. Silicon wafers were obtained from BT Electronics. The pressure controllers (model MFCS−EZ) used to inject the fluids into the microfluidic chips were purchased from Fluigent. The tubing connecting the pressure controllers to the microfluidic chip was bought from VWR (internal diameter: 0.51 mm, external diameter: 1.52 mm). The channel inlets and outlets were punched with 0.35 mm biopsy punchers delivered by World Precision Instruments (WPI), while the plasma cleaner was purchased from Harrick Scientific.

PFH and the fluorinated surfactant, Krytox 157 FSL, were purchased, respectively, from ABCR GmbH and Chemours.

Synthesis of F-TAC Surfactant. F−TAC surfactants are amphiphilic molecules composed of two structural parts (Figure 1A). One part is the polar head, made of a water-soluble oligomer of tris(hydroxymethyl) aminomethane (Tris). The second is the fluorinated tail. F−TAC surfactants are readily available at the gram scale in one step by radical telomerization of the monomer tris(hydroxymethyl)-acrylamidomethane in the presence of a telogen reagent (perfluoroalkanethiol) and a radical initiator (α,α'-azobisisobutyronile or AIBN), according to the reaction shown in Figure 1B.[22] The length of the polar head can be tuned according to the concentration of the starting reagents and conditions established for their synthesis.

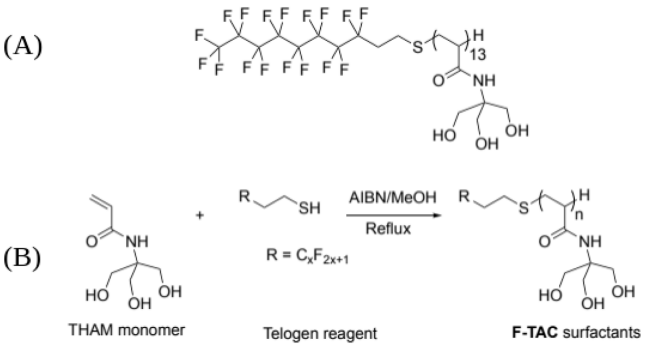

Figure 1. (A) Chemical structure of F_8−TAC_{13} surfactant. (B) General synthetic pathway of F−TAC surfactants (reagents and conditions: AIBN/CH_3OH, reflux 62−73%).

Within a perfluorocarbon emulsion, the polar head of the F−TAC surfactant is located at the surface of perfluorocarbon droplets, in contact with water, while the fluorinated tail acts as a fluorophilic anchorage ensuring the stabilization of the PFH droplets. In order to ensure an optimal droplet stabilization and water solubility, the F−TAC used in the current study is made of a fluorinated tail with eight fluorinated carbons and endowed with 13 Tris units and will be referred as "F_8−TAC_{13}" surfactant.

Interfacial Tension. The interfacial tensions were measured with an error of 2 mN/m using either a Tracker tensiometer (Teclis, France) or an SDT tensiometer (Krüss) at 20 °C (for samples with glycerol). The first instrument analyzes the shape of either a pendant PFH droplet in water or a bubble in water or liquid PFH, while the second analyzes the shape of a spinning droplet or bubble. All droplet or bubble shapes were fitted by the Young−Laplace equation in order to derive the surface or interfacial tension. Measurements were made after the value of interfacial tension reached an equilibrium value. Some measurements were performed in the presence of 0.1 wt % F_8TAC_{13} (solubilized in water or glycerol) or 5% Krytox 157 FSL (solubilized in PFH).

DROPLET GENERATION AND CHARACTERIZATION

Microfluidic Chip Fabrication. We manufactured two types of chips. The first one, suitable for the production of either plain PFH droplets or water multicore PFH droplets, uses a single classic flow-focusing chip (top and middle figures in Figure 2). In these chips, all channels are rectangular (50 μm deep and 100 μm wide), while the nozzle size is 10 and 40 μm depending on the droplet radius (see Table 1).

The second type of chips was used for the production of water single-core PFH droplets and is made of two flow-focusing junctions in series inside one chip, as shown in bottom figure of Figure 2. All channels are rectangular (50 μm deep and 100 μm wide), the size of the first nozzle is 35 μm, while the second nozzle has a size of 70 μm.

Both chip types were first designed on AutoCAD, then printed using a two-photon polymerization printer, a Nanoscribe GT Photonic Professional device with a negative-tone photoresist IP-S (Nanoscribe GmbH, Germany) and 25×

https://doi.org/10.1021/acs.langmuir.3c02272
Langmuir 2023, 39, 15716−15729

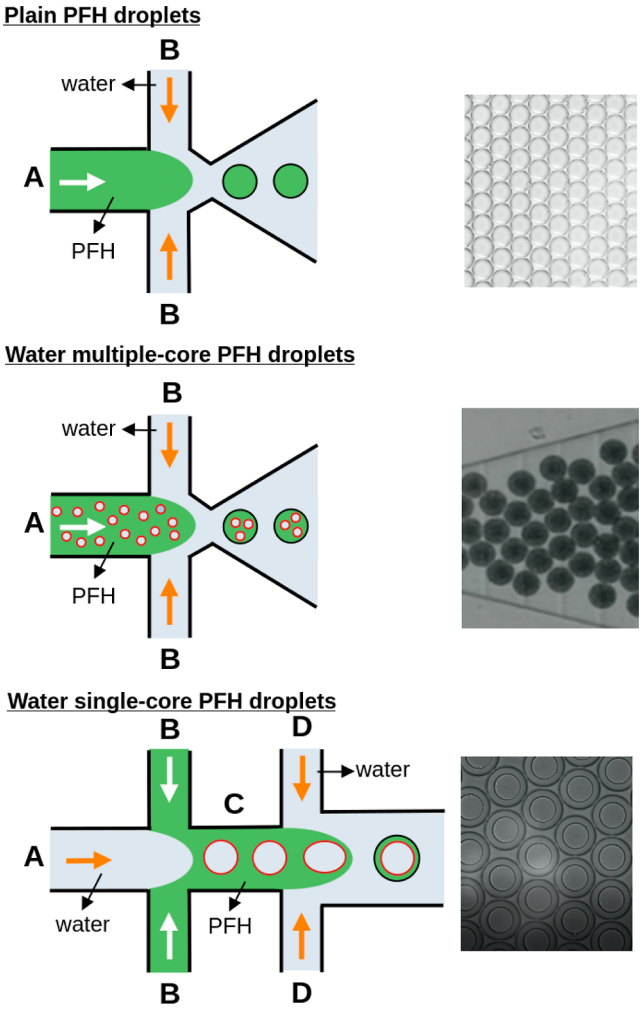

Figure 2. Schematic representation of one- (top and middle schemes) and two-nozzle (bottom scheme) microfluidic chips used to produce plain PFH droplets, water multiple core PFH droplets, and water single-core PFH droplets. The green and blue colors filling the channels are for perfluorohexane and water, respectively. The black line around the droplets indicates the presence of F_8−TAC_{13} surfactant, while the red line indicates the presence of Krytox surfactant. For each droplet type, a picture of the emulsion taken under microscope is given.

Table 1. Nozzle Diameters, Flow Rates of the Dispersed Phase Θ_d and of the Continuous Phase Θ_c Used in the Microfluidic Chip to Produce Plain PFH Droplets of Radius *R*

R (μm)	Θ_d (μL/min)	Θ_c (μL/min)	nozzle size (μm)
2.5	0.3	0.8	10
5	0.9	8	10
20	0.9	8	40
30	1	2.5	40

objective, directly on silicon substrates after a nitrogen plasma cleaning preparation (to increase the resin adhesion on the substrate). To reduce printing time, a shell writing strategy was applied. It consists of fabricating a dense shell delimiting the structure, the inner being only partly polymerized in the form of a scaffold. After developing in propylene glycol methyl ether acetate (for 30 min) and isopropanol (for 5 min), batch polymerization is performed with UV-exposure. Soft lithography was then used to replicate the channels. PDMS and its cross-linking agent were mixed at a ratio of 10:1 (w/w), degassed, and poured onto the mold. The polymer was cured for 2 h at 70 °C. PDMS chips were then peeled off carefully from the mold, and 350 μm holes were punched into the chip with biopsy punchers to create the inlets and outlets. Once the design was etched onto the PDMS, the patterned surface of the chip and the surface of a glass slide were activated in a plasma cleaner filled with air for 1 min at a power of 18 W. This plasma activation ensures the secure bonding of the chip on the glass slide. The walls of the channels constituting the single flow-focusing junction chip were treated hydrophilic. To do this, the chip was plasma activated for 1 min, and water was passed through the channels.

Production of Plain PFH Droplets. We used two distinct methods to generate PFH droplets depending on their size. In both methods, the mass ratio of F_8−TAC_{13} to continuous aqueous phase was 0.1%.

Plain PFH droplets with a nanometer-sized radius were produced using a high-pressure homogenizer (model LV1 from Microfluidics). For this technique, a coarse emulsion was first prepared by vortexing. The coarse emulsion was then used with the high-pressure homogenizer, where the emulsion went at a high velocity (thanks to a high-pressure pump) through two capillaries, which met inside a Y-shaped chamber (model F12Y, internal dimension of 75 μm). The high shear forces occurring in this chamber between the two emulsion flows induce a reduction in the droplet size. The passage through the chamber was repeated 8 times at a pressure of 138 MPa. The resulting emulsion was centrifuged at 6000 rpm (i.e., at a relative centrifugal force of 2000*g*) for 30 s using a bench mini-centrifuge (Mini Star from VWR) to force any droplets with diameter larger than 1 μm to sediment, and only the supernatant was kept.

Plain PFH droplets with a micron-sized radius were generated by microfluidics using a conventional single flow-focusing chip, where the flow rates of the dispersed phase (channel filled with PFH, white arrow in the top figure of Figure 2) and of the continuous phase [channel filled with the aqueous solution solubilizing F_8−TAC_{13} (orange arrows in the top figure of Figure 2)] are given in Table 1.

Production of Water Single-Core PFH Droplets. These droplets were produced using a two-nozzle device (see Figure 2). Following the procedure of Bodin-Thomazo et al.,[23] the channel making the junction between the PFH and water channels (i.e., channel C between channels B and D in Figure 2), was selectively patterned using a black marker to avoid the wetting of the walls by PFH. We used a flat PDMS layer as a substrate for the chip instead of a glass slide. This was followed by the surface treatment procedure previously explained (air plasma for 1 min). After the treatment, the chip and the flat PDMS were aligned to fit the marker pattern. In this chip, the walls of the unpatterned channels remain hydrophilic, while the walls of the patterned channel are kept hydrophobic. The chip was first flushed with methanol, and then, flushed with water for 20 min before starting the production of droplets. Then, the different fluid phases (PFH and aqueous solutions) were injected into the microfluidic device by applying a pressure of 20 mbar to the headspace of their respective inlets. The flow rates were adjusted to encapsulate exactly one water droplet in each double emulsion within these ranges: 0.8−2.3 μL/min for the dispersed aqueous phase (orange arrow in channel A on the bottom figure of Figure 2), 1−5.5 μL/min for

https://doi.org/10.1021/acs.langmuir.3c02272
Langmuir 2023, 39, 15716−15729

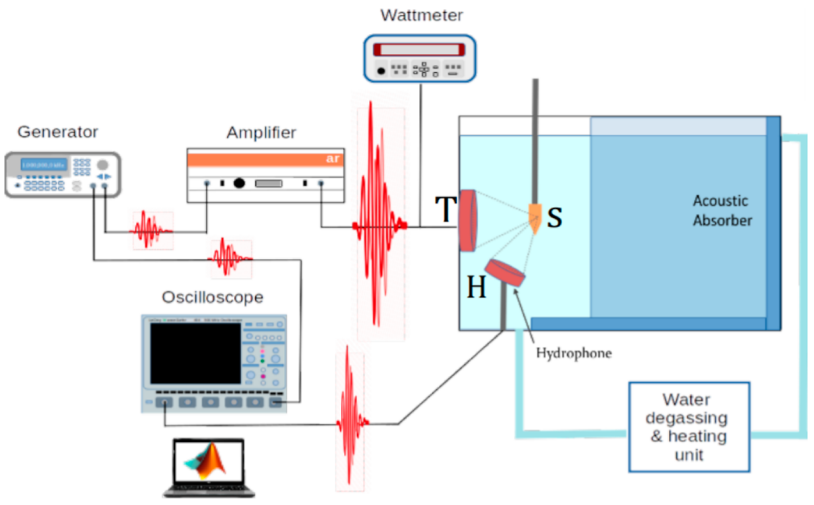

Figure 3. Experimental setup for ADV and measuring cavitation. A 1.1 MHz transducer (T) vaporized the droplets while the hydrophone (H) recorded at 0.55 MHz the scattered emissions due to subharmonic response of vapor microbubbles in the sample (S).

the intermediate PFH phase (white arrows in channels B), and 2−8 μL/min for the continuous aqueous phase (orange arrows in channels D).

Production of Water Multicore PFH Droplets. A coarse emulsion of water in PFH was first produced inside a vial from a mixture of normal saline (0.9 wt % NaCl), PFH, and Krytox (5 wt %). The ratio of normal saline to PFH was adjusted depending on the desired water volume fraction inside a multicore droplet. The coarse emulsion was obtained by sonication using a Branson digital Sonifier (model 450) with a double step microtip at a frequency of 20 kHz, 30% of maximum amplitude for a pulse of 5 s, and a 10 s pause, for 2 min. During sonication, the vial containing the fluids was immersed in an ice−water bath to avoid the vaporization of PFH due to the heating generated during the process. An emulsion made of normal saline nanodroplets surrounded by Krytox 157 FSL and dispersed in the PFH was thus produced.

In the next step, the multicore droplets were generated in the same flow-focusing chip as the one used for a plain droplet generation, with the above primary nanoemulsions as the dispersed phase and water as the continuous phase. The resulting multicore droplet therefore consists of multiple aqueous nanodroplets inside a larger PFH droplet surrounded by water. We define φ_w as the volume fraction of water composing a droplet and R_w as the mean radius of the water droplets encapsulated inside the PFH droplets.

The flow rates used to produce these emulsions are in the same ranges as the ones used for plain PFH droplets.

Size and Polydispersity Measurements. For micron-sized droplets, the size and polydispersity were estimated from a series of videos taken with an ultrafast camera (model SC1, Edgertronic, USA) during their production. The collected recordings were treated with an in-house MATLAB program. The code uses a Circular Hough Transform-based algorithm for locating the droplets and then estimating their diameter along with the polydispersity index (PDI). This approach was chosen owing to its robustness in the presence of noise, occlusion, and varying illumination. An example is given in Figure S1 for water single-core droplets, where the inner radius (R_w) and outer radius (R) diameter were extracted using MATLAB. The water volume fraction φ_w was derived from R_w and R for water single-core PFH droplets.

For PFH nanodroplets dispersed in water (and stabilized by F_8−TAC_{13}) or for water nanodroplets dispersed in PFH (and stabilized by Krytox) before their encapsulation into PFH droplets, the size and polydispersity were determined by dynamic light scattering. The measurements were performed on emulsions diluted 100 times using an ALV/CGS-3 platform-based goniometer system (from ALV GmbH) at room temperature. An experiment consists of measurements of the same solution at scattering angles, θ, ranging from 50 to 160°, with a step of 10°. At each angle θ, the device provides the decay rate $\Gamma_\theta = q^2 \frac{k_B T}{6\pi\eta R}$, where k_B is the Boltzmann constant, T is the temperature in K, η is the viscosity of the solvent, and $q(\theta) = (4\pi n_s/\lambda)\sin(\theta/2)$ is the magnitude of the scattering vector. The refractive index of the solvent is n_s = 1.33, and λ = 633 nm is the laser wavelength. A fit of the curve by the cumulant method made it possible to determine the hydrodynamic droplet mean radius R along with the PDI.[24] A typical example of Γ_θ versus q^2 plot is presented in Figure S2 for plain PFH droplets, which exhibit a diameter of 149 nm.

■ ADV EXPERIMENTS

Acoustic Setup. Figure 3 provides the sketch of the ultrasonic setup triggering the ADV. A waveform generator (model 33220A from Agilent) generates an electrical signal that first goes through a radio frequency power amplifier (model 150A100C from AR France) and then through a power reflection meter (Model NRT from Rohde Schwarz) that measures the delivered average electrical power. The electrical signal is converted into an acoustic wave by a focused transducer (Model H-101-G from Sonic concepts Inc., with an f-number of 0.99), whose fundamental mode is at 1.1 MHz. The acoustic wave propagates into a water tank thermostated at 20 ± 0.2 °C and connected to a degassing machine (Model WDS-1005 from Sonic Concepts), which reduces the concentration of dissolved oxygen below 2 mg/L. A polymerase chain reaction (PCR) tube filled with 200 μL of suspension is placed at the transducer focus. A hydrophone (model Y-107 from Sonic Concepts), whose focus overlaps with that of the transducers inside the tube, continuously monitors the scattered signal.

https://doi.org/10.1021/acs.langmuir.3c02272
Langmuir 2023, 39, 15716−15729

The positioning of the PCR tube at the transducer focus was performed using a 0.2 mm needle hydrophone (from Precision acoustics) placed inside an open tube. The transducer was made to emit long and low-intensity acoustic pulses, and the amplitude of the output signal was monitored and recorded by the hydrophone. The tube/hydrophone position was varied, thanks to x-y-z motored stages, and we selected the position corresponding to the maximum amplitude recorded by the hydrophone to place the tube at the focal point.

In addition, we used a Fabry−Pérot fiber-optic ultrasonic hydrophone (Precision Acoustics, Dorchester, UK) for the measurement of temperature.[25] In our case, temperature variations never exceeded 0.5 °C at the applied pressures.

Acoustic Parameters. The signal consisted of sine-wave bursts at a fundamental frequency of 1.1 MHz. We employed short bursts of 5-cycle sine wave gated by a rectangular window of 91 μs pulses at an interval of 3 s to allow sufficient time to record the output. To subsidize any thermal effects, we fixed the duty cycle at 5% and the pulse repetition frequency at 11 kHz. The total time of an experiment was 7 min. Acoustic peak negative pressures varied from $|P|$ = 0.3 to 7 MPa.

Sample Preparation. Due to their high density, the droplets sediment quickly when dispersed in water. In order to guarantee a homogeneous dispersion of the droplets during the duration of the experiment, glycerol was chosen as the bulk phase because of its viscosity of 11.1 mPa s.

The samples were prepared by taking, for instance, a volume of v = 0.1 μL from the bottom of a solution of droplets in water (so that the pipetted volume is mostly made of droplets) and by dispersing it in a volume of 200 μL of degassed glycerol in a PCR tube. In this case, the volume fraction of the droplets was approximately $\varphi_d = 5 \times 10^{-4}$. Other values of φ_d were obtained by varying the volume v of the droplets added to 200 μL of glycerol. To ensure a homogeneous distribution of the droplets before each experimental test, the tube was vortexed at 2000 rpm for 30 s. Table 3 lists the different sizes and the corresponding numbers of droplets dispersed in 200 μL of glycerol solution. A solution of fresh droplets was prepared before each experiment.

Table 2. Values of Interfacial Tensions, Where the Subscripted Letters g, l, c, w Are for Gaseous PFH, Liquid PFH, Glycerol, and Water, Respectively[a]

notation	interfacial tension (N/m)	surfactant
γ_{gl}	0.012	none
γ_{lc}	0.014	F_8−TAC_{13}
γ_{gc}	0.033	F_8−TAC_{13}
γ_{lw}	0.018	Krytox 157 FSL
γ_{gw}	0.066	Krytox 157 FSL
γ_{gw}	0.072	none
γ_{lc}	0.026	none
γ_{gc}	0.062	none
γ_{lw}	0.025	F_8−TAC_{13}
γ_{gw}	0.038	F_8−TAC_{13}

[a]The first five values are of interest for our configuration. The next five values are controls or intended as a comparison between water and glycerol. The error in the values is ±0.002 N/m.

ADV Signal Processing. The method of measuring the ADV threshold is based on the principle that microbubbles (i.e., vaporized droplets) are much more powerful acoustic scatterers than liquid droplets because of the high compressibility of gases compared to that of liquids.[26,27] When excited at a given frequency f_0, a bubble oscillates not only at this same resonant frequency but also at the subharmonic $f_0/2$[28] and at higher harmonics if_0 (where i is an integer larger than 1). However, higher harmonics if_0 can also appear due to the nonlinear propagation of an acoustic wave.[29] Hence, the appearance and magnitude of the subharmonic peaks at half the fundamental frequency, here $f_0/2$ = 0.55 MHz, were used as the most relevant indicator to detect the onset of ADV. For instance, Figure S3A displays the signal emitted by a glycerol solution containing plain PFH droplets with a radius of 20 μm that were insonified by a sound wave of amplitude 2 MPa, sufficient enough to trigger ADV. This is evidenced by the magnified level of the subharmonic at 0.55 MHz (gray solid line) in Figure S3 B compared to pure glycerol (black dotted line).

The determination of the ADV threshold can be achieved using two methods that will be compared to each other hereafter. To do so, three different samples were used for each experiment. For each sample, the amplitude of the emitted signal was progressively increased, at 25 mV intervals, at the waveform generator. For each increment, the pressure wave scattered by the droplets was collected by the hydrophone. 100 pulses were sent onto each sample, leading to the recording of 100 scattered signals, which were then stored for each sample at each applied pressure. During acquisition, the oscilloscope performed analog-to-digital conversion of the signal at a sample rate of 1 GHz. Once recorded, the fast Fourier transform (FFT) of each acquired signal was calculated using MATLAB. Therefore, the data points in the charts shown in this article are all averages over 300 FFT data.

Method A. We first derived the FFT spectra of the signal emitted from a droplet sample at an applied acoustic pressure P. Then, we calculated the power spectrum V_{sub} around the subharmonic peak $f_0/2$ (from 0.4 to 0.6 MHz). According to Maxwell et al.,[30] the value of V_{sub} depends linearly on pressure in the absence of cavitation (or vaporization). Consequently, we normalized the value V_{sub} by the applied pressure times a constant so that a plateau appeared at low pressures. Any deviation from this plateau would be characteristic of the occurrence of cavitation. The data points were fitted using a piecewise linear function (see Figure 4). The pressure at the intersection point of the two linear fits indicated the ADV threshold.[4,31,32]

Method B. The differentiation between the presence and absence of bubble formation is made by taking the integral I of the Fourier Transform (IFT) in the subharmonic range between 0.4 and 0.6 MHz[3,10] of the droplet sample $I_{vap}(P)$ and a control sample of glycerol $I_{gly}(P)$ containing no droplets at each applied pressure. Vaporization occurrence at a particular acoustic pressure P was determined according to the criterion

$$I_{vap}(P) \geq I_{gly}(P) + \zeta\sigma \quad (1)$$

where ζ is an integer and σ is the standard deviation value of the values of $I_{gly}(P)$ recorded from glycerol at pressure P compared to its mean value. Each time the condition in eq 1 was met, a vaporization event was counted. As the phenomenon is stochastic, its probability, $p^{(n)}$, was obtained by repeating the experiment 100 times at the same pressure value and for the same sample. The probability, $p^{(n)}$, of bubbles appearing within a sample for a given pressure P was defined as the frequency of vaporization, i.e., the sum of vaporization events observed divided by 100. This value was then averaged

https://doi.org/10.1021/acs.langmuir.3c02272
Langmuir 2023, 39, 15716−15729

Table 3. Results from Experiments Performed on a Solution of PFH Plain Droplets Dispersed in Glycerol at a Droplet Volume Fraction $\varphi_d = 5 \times 10^{-4}$[a]

R (μm)	n_{tot}	n	$\lvert P_{0.5}^{(n)}\rvert$ (MPa)	$\lvert P_{0.5}^{(1)}\rvert$ (MPa)	σ^1 (MPa)
0.1	2.4×10^{10}	4.5×10^{7}	2.51 ± 0.02	8.5 ± 0.6	1.08 ± 0.11
2.5	1.5×10^{6}	2.9×10^{3}	2.42 ± 0.01	5.8 ± 0.2	0.86 ± 0.05
5	1.9×10^{5}	3.6×10^{2}	2.39 ± 0.01	4.9 ± 0.2	0.86 ± 0.05
20	2.9×10^{3}	6	2.12 ± 0.01	3.1 ± 0.1	0.75 ± 0.09
30	8.8×10^{2}	2	1.41 ± 0.01	1.5 ± 0.1	0.21 ± 0.01

[a]R is the radius of the droplets, and n_{tot} is the total number of droplets in the sample tube, while n is the number of droplets inside the acoustic focus volume (determined at −6 dB). $P_{0.5}^{(1)}$ and $P_{0.5}^{(n)}$ are the derived pressure at which the probability to observe a vaporization event is 0.5, when 1 or n droplets are respectively present in the acoustic focus volume. σ^1 is the standard deviation on the gaussian distribution having $P_{0.5}^{(1)}$ as a median.

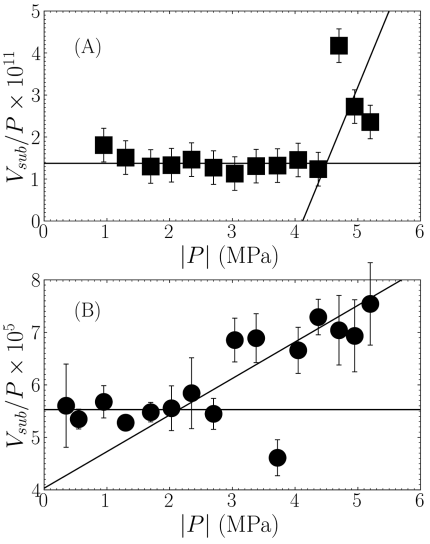

Figure 4. Normalized subharmonic component peak amplitude of the scattered response of a glycerol solution devoid of droplets (A) and of a suspension of PFH droplets (R = 20 μm, $\varphi_d = 5 \times 10^{-4}$) in glycerol (B) as a function of applied acoustic pressure P. The two lines intersect to give $|P|$ = 4.5 ± 0.3 MPa for the (A) and $|P|$ = 2.1 ± 0.3 MPa for the figure (B). Consequently, the vaporization of the PFH droplets appears before glycerol cavitation when pressure increases.

over three independent experiments using three different samples.

We assumed that, in our suspension of droplets, each droplet vaporizes independently of the other with a probability $p^{(1)}$. The number of vaporization events from n droplets is then given by a binomial distribution with parameters n and $p^{(1)}$ and the probability to observe at least one vaporization by

$$p_{\geq 1}^{(n)} = 1 - [1 - p^{(1)}]^n \quad (2)$$

When n becomes large, $p_{\geq 1}^{(n)}$ is approximated by a minimal Gumbel distribution with location parameters $\mu^{(n)}$ and scale parameters $\beta^{(n)}$

$$p_{\geq 1}^{(n)} \approx 1 - \exp[-e^{(P-\mu^{(n)})/\beta^{(n)}}] \quad (3)$$

The median of this distribution is $P_{0.5}^{(n)}$ and can be expressed as

$$P_{0.5}^{(n)} = \mu^{(n)} + \beta^{(n)}\ln(\ln(2)) \quad (4)$$

The probability $p^{(n)}$ to observe a vaporization event when n droplets are insonified is fitted by eq 3 to obtain the value of $P_{0.5}^{(n)}$ (using eq 4). However, the determination of the $P_{0.5}^{(n)}$ value depends on the chosen value for ζ.[3] It is expected that when ζ is low, fluctuations of the background, at $f_0/2$, may contribute to the events ascribed to vaporization, which is introducing a bias in $P_{0.5}^{(n)}$ determination. In contrast, if ζ is large, we may fail to detect the vaporization events. Figure 5 displays the

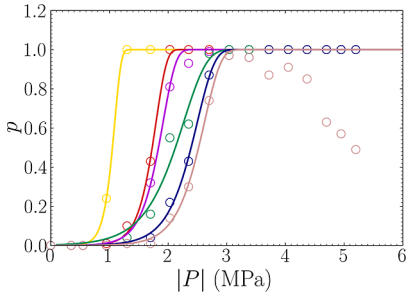

Figure 5. The probability $p^{(n)}$ to detect an ADV event was evaluated as a function of the applied peak negative acoustic pressure P using different values for ζ (3, 5, 6, 7, 9, and 10 from the left to the right probability curves). From the respective curves, we determined the following $P_{0.5}^{(n)}$ values: 1.0, 1.7, 1.8, 2.1, and 2.4 MPa. The experiments were performed on a suspension of plain PFH droplets having a radius R = 20 μm and at a droplet volume fraction $\varphi_d = 5 \times 10^{-4}$.

probability curves determined for a suspension of plain PFH droplets (R = 20 μm and $\varphi_d = 5 \times 10^{-4}$) for ζ varying from 5 to 10. For ζ = 10, some vaporization events are obviously missed as p does not remain on a plateau after reaching 1. A plateau at p = 1 is rapidly reached when ζ = 3, 5 and 6, compared to larger values of ζ, suggesting that signals not associated with a vaporization event are taken into account in the derivation of p. We thus chose a value of 7 for ζ as it was the value exhibiting no bias when considering our whole experimental data, while at ζ = 9, a decrease in the plateau at 1 could be observed in some of our experiments.

RESULTS AND DISCUSSION

Interfacial Tensions. Several interfaces are at play in our system, each of them characterized by an interfacial tension γ. Since nucleation models depend on these interfacial tensions, we measured their values (given in Table 2) at equilibrium for all the configurations met in our droplet systems. This includes the interfacial tensions between liquid PFH and glycerol (γ_{lc}), liquid PFH and water (γ_{lw}), gaseous PFH and glycerol (γ_{gc}), gaseous PFH and water (γ_{gw}), and finally gaseous and liquid PFH (γ_{gl}). Note that our value for γ_{gl} is very close to the one measured by Luís et al.[33] (that is 11.7 mN/m). The values were measured in the presence of F_8−TAC_{13} when using glycerol or in the presence of Krytox 157 FSL when using water. Since droplets are of millimetric size in these experiments, the measured values are close to those of a flat

https://doi.org/10.1021/acs.langmuir.3c02272
Langmuir 2023, 39, 15716−15729

surface (i.e., $R \approx \infty$), and we consider that $\gamma_{lc} = \gamma_{lc}(\infty)$, $\gamma_{lw} = \gamma_{lw}(\infty)$, $\gamma_{gc} = \gamma_{gc}(\infty)$, $\gamma_{gw} = \gamma_{gw}(\infty)$, and $\gamma_{gl} = \gamma_{gl}(\infty)$.

However, the effective interfacial tension is significantly different from these values for droplets with a radius of several hundreds of Angström according to Tolman[34]

$$\gamma(r) = \frac{\gamma(\infty)}{1 + \frac{2\delta}{r}} \tag{5}$$

where r is the radius of the droplet, $\gamma(\infty)$ is the interfacial tension for a flat interface (i.e., $r = \infty$), and δ is the Tolman length, whose value is on the order of a few Angström.[35] Consequently, we expect γ_{gw} and γ_{gl} to strongly depend on the nucleus size, while γ_{lw} should not significantly vary because $\delta/R \ll 1$ in the experimentally explored range of droplet radii.

Cavitation Pressure Threshold in Glycerol. The pressure threshold that induces cavitation in pure glycerol was evaluated in the absence of droplets. In these experiments, all glycerol solutions were vortexed at a speed of 2000 rpm for 30 s before measurements. Using the Method A described in the section "ADV signal processing", we measured the normalized subharmonic peak amplitude of the acoustic signal of pure glycerol for an acoustic peak negative pressure P, whose absolute value increases from 1 to 5.2 MPa, as shown in Figure 4A. In these experiments, a different glycerol solution was used for each measurement. We observe from Figure 4B that cavitation starts to occur for $|P| > 4.5$ MPa in pure glycerol. Consequently, all of our measurements on determining the ADV pressure threshold were performed at $|P| < 4.5$ MPa, hence, in the absence of cavitation occurring in glycerol.

Assessment of the Absence of Superharmonic Focusing. We followed the procedure described by Shpak et al.[36] We first used the software HIFU-beam Simulator[37] to evaluate the shape of the acoustic wave produced by our transducer in the absence of droplets. In this Matlab script, we used as input parameters, the frequency (f = 1.1 MHz), the geometric focus (63.2 mm), and radius (64.00 mm) of our transducer, as given by the manufacturer Sonic Concepts. The acoustic pressure wave was evaluated at the transducer focus and then fitted by a Fourier series[36]

$$P_0(t) = \sum_{n=0}^{\infty} a_n e^{i(n\omega t + \phi_n)} \tag{6}$$

where $\omega = 2\pi/f$, ϕ_n is a phase term, and a summation up to 10 was more than enough to fit the acoustic wave. We used the values a_n and ϕ_n to evaluate the contribution to the acoustic pressure P_d due to the presence of the droplet[36]

$$P_d(r, \theta, t) = \sum_{n=0}^{\infty} \sum_{m=0}^{\infty} a_n e^{i(n\omega t + \phi_n)} \alpha_{mn} j_m(nk_1 r) P_m(\cos\theta) \tag{7}$$

where j_m is the spherical Bessel function of the first kind of order m, P_m is the Legendre polynomial of order m, and

$$\alpha_{mn} = \chi_m \frac{j_m(x_0) h_m^{(2)\prime}(x_0) - h_m^{(2)}(x_0) j_m'(x_0)}{j_m(x_1) h_m^{(2)\prime}(x_0) - \frac{k_1\rho_0}{k_0\rho_1} h_m^{(2)}(x_0) j_m'(x_1)} \tag{8}$$

where $\chi_m = (-i)^m(2m + 1)$, $x_0 = nk_0R$, $x_1 = nk_1R$, and $h_m^{(2)}$ is the spherical Hankel function of the second kind of order m. Using eq 7, we looked at the moment, where the pressure reached its minimum value inside the droplet. For all combinations of droplet radius and acoustic pressure tested in our experiments, we observed no superharmonic focusing. An example of curve snapshot for the largest droplet radius (of 30 μm) is given in Figure S4.

Methods to Determine ADV Pressure Threshold ($P_{0.5}$). We performed measurement on solutions of plain PFH droplets with a radius of 20 μm. We used Method A and B to determine the value $P_{0.5}^{(n)}$ of ADV pressure threshold. Figure 4B shows that Method A gave the value $|P_{0.5}^{(n)}| = 2.1 \pm 0.3$ MPa, which is at the point of intersection of the linear piecewise fit. However, Method B yielded $|P_{0.5}^{(n)}| = 2.12 \pm 0.03$ MPa as shown in Figure 5 from the fit of the data to eq 3 and the use of eq 4. Consequently, both methods gave similar ADV threshold values $P_{0.5}^{(n)}$. The error obtained by Method B was noticeably smaller than Method A, and for this reason, we used Method B to derive the probability of vaporization in the following experiments. Note that the number of detected vaporization events associated with the droplets is expected to be much smaller than the number of cavitation events occurring in glycerol. Thus, while the precision of Method A is adequate to detect cavitation in glycerol, the precision of Method B is more adapted for the detection of the vaporization event.

$P_{0.5}$ as a Function of Plain PFH Droplet number (n). We performed measurements on solutions of plain PFH droplets, whose radii were 20 μm, for droplet volume fractions φ_d varying from 2.5×10^{-4} up to 50×10^{-4}. From these measurements, we derived the ADV pressure threshold $P_{0.5}^{(n)}$ using Method B. In these experiments, only the droplets located in the volume v_{focus} of the transducer focus may be vaporized. This volume is equal to 0.38 μL (determined at −6 dB according to the manufacturer specifications) and contained n = 3, 6, 11, 28, and 57 droplets for φ_d equal to 2.5×10^{-4}, 5×10^{-4}, 10×10^{-4}, 25×10^{-4}, and 50×10^{-4}, respectively. We observe in Figure 6A that the probability curves are shifted upon the addition of droplets. The fit of these probability curves provides the values of $P_{0.5}^{(n)}$, displayed in Figure 6B, which represents the values of pressure at which the probability to observe an ADV event is $p^{(n)} = 0.5$. The value of $|P_{0.5}^{n}|$ decreases as the number of insonified droplets n increases.

$P_{0.5}$ as a Function of Plain PFH Droplet Radius (R) at a Constant Droplet Volume Fraction (φ_d). The next measurements were performed at a constant volume fraction of plain droplets, $\varphi_d = 5 \times 10^{-4}$, irrespective of the droplet radius. The droplets have a radius of either 0.1, 2, 5, 20, or 30 μm. As a consequence, the number of droplets n located in the volume of the transducer focus varied. We calculated that n was respectively equal to 4.5×10^7, 2.9×10^3, 3.6×10^2, 6, and 2 droplets. For each radius, we determined the probability $p^{(n)}$ to observe a vaporization event as a function of the acoustic peak negative pressure P. From these probability curves, we derived $P_{0.5}^{(n)}$, whose values are displayed in Table 3 and Figure 7. The values slightly decrease as the droplet radius increases, while the volume droplet fraction is constant (i.e., the corresponding number of droplets increases).

$P_{0.5}$ as a Function of Volume Fraction of Encapsulated Water (φ_w) in Multicore PFH Droplets. We performed experiments with suspensions of PFH droplets (of radius R = 20 μm and of volume fraction $\varphi_d = 5 \times 10^{-4}$) composed of many water droplets (of radius R_w = 0.215 μm). The concentration of water droplets was varied so that the volume fraction of water in a droplet φ_w ranges from 0.2 to 0.8. The ADV pressure thresholds, determined for the various

https://doi.org/10.1021/acs.langmuir.3c02272
Langmuir 2023, 39, 15716−15729

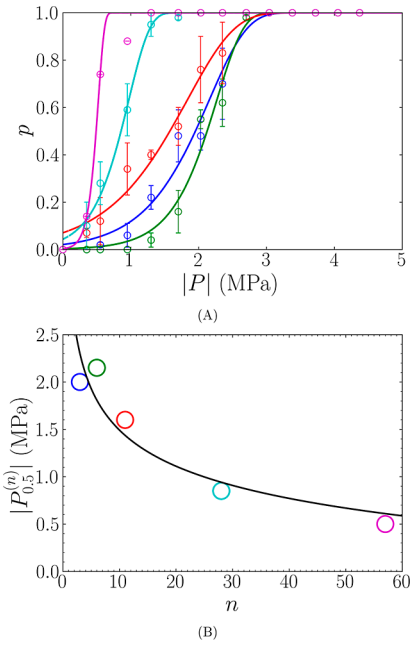

Figure 6. (A) The circles represent the probability p to measure a vaporization event as a function of pressure for solutions containing droplets of radius 20 μm and at various droplet volume fractions φ_d (see text), leading to a number of droplets in the transducer focus of 3 (blue circles), 6 (green circles), 11 (red circles), 28 (cyan circles), and 57 (magenta circles). The lines are fits performed using either eq 3 or 13 as there is no difference between the two fits. (B) The values $|P_{0.5}^{(n)}|$ obtained from the previous fit are plotted as a function of n, the number of droplets localized in the transducer focus. The line is a fit (R^2 = 0.88) using eqs 13, 11, and 12, for which $|P_{0.5}^{(1)}|$ = 3.3 ± 0.4 MPa and $\sigma^{(1)}$ = 1.2 ± 0.3 MPa.

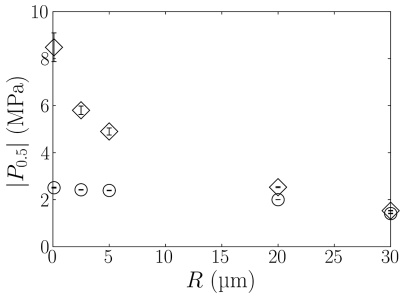

Figure 7. Values of $|P_{0.5}^{(1)}|$ (◇) and $|P_{0.5}^{(n)}|$ (○) determined for solutions at a constant volume fraction of droplets ($\varphi_d = 5 \times 10^{-4}$) with the droplet radius varying from 0.1 to 30 μm.

values of φ_w, are displayed in Figure 8 along with the value for plain PFH droplets, which correspond to $\varphi_w = 0$. We observe that the values of $|P_{0.5}^{(n)}|$ vary around 2.2 MPa (dotted line in Figure 8) for the water multicore PFH droplets, close to the value $|P_{0.5}^{(n)}|$ for plain PFH droplet when $\varphi_d = 5 \times 10^{-4}$.

$P_{0.5}$ between Water Single-Core and Multicore PFH Droplets. In the following experiments, we consider suspensions of droplets (of radius R = 20 μm and of volume concentration $\varphi_d = 5 \times 10^{-4}$) made of a single water droplet (of radius R_w = 10.5 μm). The water volume fraction is $\varphi_w \approx$ 0.15. We derived a value of $|P_{0.5}^{(n)}| = 1.6 \pm 0.1$ MPa from our probability curve, and the value is plotted in Figure 8 in order to compare it with the values determined for multicore water

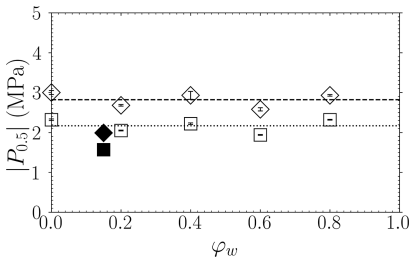

Figure 8. The squares represent the values of $|P_{0.5}^{(n)}|$ for a suspension of either water multicore PFH droplets (□) or water single-core PFH droplets (■). However, the lozenges represent the values of $|P_{0.5}^{(1)}|$ for a suspension of either water multicore PFH droplets (◇) or water single-core PFH droplets (◆). All suspensions contain an identical droplet volume fraction of $\varphi_d = 5 \times 10^{-4}$ and an identical radius of R = 20 μm. The water droplets are stabilized by Krytox 157 FSL and possess a radius of either R_w = 10.5 μm or 250 nm when a PFH droplet contains, respectively, a single water droplet (■ and ◆) or many of them (□ and ◇).

PFH droplets. We observe that the value $|P_{0.5}^{(n)}|$ is much smaller for water single-core droplet than for multicore ones.

Extrapolating ADV Pressure Threshold from a Suspension of Insonified Droplets to a Single Insonified Droplet. Since experiments were performed on droplet suspensions, the value $P_{0.5}^{(n)}$ should depend on the number of insonified droplets and therefore be different from the value $P_{0.5}^{(1)}$ that would be obtained if only one droplet was insonified. Our experiments on an increasing concentration of plain PFH droplets of radius 20 μm confirmed the dependence of $P_{0.5}^{(n)}$ on n (see Figure 6B). This result means that comparisons between different measurements can be drawn only if they were performed at the same number of insonified droplets. This is a critical point as most experiments in the literature do not specify or control this number.

To understand the ADV mechanism, it is crucial to determine the value of $P_{0.5}^{(1)}$ instead of $P_{0.5}^{(n)}$ as all nucleation models to date were developed for the case of one droplet. It is possible to achieve this either by diluting the droplet solution until we reach $P_{0.5}^{(1)}$ or by directly calculating the value $P_{0.5}^{(1)}$ from the probability curves $p^{(n)}$. Indeed, it can be shown that if the probability $p^{(1)}$, which is a function of acoustic pressure P, is given by an integral Gaussian distribution with median $P_{0.5}^{(1)}$ and standard deviation $\sigma^{(1)}$, then $\mu^{(n)}$ and $\beta^{(n)}$ (given in eq 4) can be expressed as

$$\mu^{(n)} = P_{0.5}^{(1)} - \sigma^{(1)} d_n \tag{9}$$

and

$$\beta^{(n)} = \sigma^{(1)} c_n \tag{10}$$

with

$$c_n = \frac{1}{\sqrt{2\ln(n)}} \tag{11}$$

and

$$d_n = \sqrt{2\ln(n)} - \frac{\ln(\ln(n)) + \ln(4\pi)}{2\sqrt{2\ln(n)}} \tag{12}$$

By replacing the value of $\mu^{(n)}$ given by eq 9 in 3 we also obtain a relation between $P_{0.5}^{(n)}$ and $P_{0.5}^{(1)}$

https://doi.org/10.1021/acs.langmuir.3c02272
Langmuir 2023, 39, 15716−15729

$$P_{0.5}^{(n)} \simeq P_{0.5}^{(1)} - \sigma^{(1)}[d_n + c_n \ln(\ln(2))] \quad (13)$$

Equation 3 can be used to fit probability curves in order to determine either $P_{0.5}^{(1)}$ or $P_{0.5}^{(n)}$, when using respectively eqs 9−12 or 4. However,eq 13 can be used to extrapolate the value of $P_{0.5}^{(1)}$ from $P_{0.5}^{(n)}$ values determined at different n. In another words, we can extrapolate the value of $P_{0.5}^{(1)}$ through two methods: the first one by fitting $P_{0.5}^{(n)}$ values determined at several droplet concentrations or by fitting a probability curve at a known n.

Using the first method, the fit of the $P_{0.5}^{(n)}$ values illustrated in Figure 6B leads to $|P_{0.5}^{(1)}| = 3.3 \pm 0.4$ MPa (and $\sigma^{(1)} = 1.1 \pm 0.3$ MPa). While for the second method, an average value of $|P_{0.5}^{(1)}| = 3.1 \pm 0.5$ MPa (and $\sigma^{(1)} = 1.0 \pm 0.3$ MPa) is obtained from the fit of all the probability curves depicted in Figure 6A, except for $n = 57$ (i.e., magenta curve), where the probability curve could not be correctly fitted. Both these methods are therefore equivalent in providing a value for $P_{0.5}^{(1)}$. However, the second method offers the advantage of requiring the estimation of just a single probability curve for only one value of n.

We used results collected from the experiments performed at a constant volume fraction of droplet but with various droplet radii (see Figure 7), to derive $|P_{0.5}^{(1)}|$ in order to compare our data with nucleation models. We observe that the values of $|P_{0.5}^{(1)}|$ and $|P_{0.5}^{(n)}|$ are very different when n is very large but they converge to the same value where $n = 3$. It is notable that the values of $|P_{0.5}^{(1)}|$ decreases from 8.5 down to 1.5 MPa when the droplet radius increases from 0.1 to 30 μm. A correct model of nucleation should be able to predict this variation.

Failure of the Homogeneous Nucleation Model to Predict Our Results. In a homogeneous nucleation, a nucleus appears randomly inside the droplet volume. The probability $q_{\geq 1}$ that at least 1 nucleus appears is given by

$$q_{\geq 1} = 1 - e^{-N(\tau)} \quad (14)$$

where $N(\tau)$ is the average number of nucleus during a time τ and within a volume V. This can be expressed as $N(\tau) = JV\tau$, J being the volumic rate of nucleation $J = J_0 e^{-W^{hom}(q_{\geq 1})/k_B T}$ and J_0 a constant.[38] Consequently, we have

$$W^{hom}(q_{\geq 1}) = k_B T \ln\left(\frac{J_0 V \tau}{\ln\left(\frac{1}{1 - q_{\geq 1}}\right)}\right) \quad (15)$$

We suppose that the vaporization occurs during the half period where the acoustic pressure is negative, thus $\tau = \frac{1}{2f}$. In addition, the energy required to create a spherical gas volume, so-called nucleus, of radius r is[38,39]

$$W^{hom}(r) = 4\pi r^2 \gamma_{gl}(r) - \frac{4}{3}\pi r^3 (P_g - P_l) + n_{PFH}(\mu_g - \mu_l) \quad (16)$$

where γ_{gl} is the surface tension of the nucleus surface (interface between gas and liquid), P_g and P_l are the pressures in the gaseous and liquid PFH, respectively, n_{PFH} is the number of PFH molecules, and μ_g and μ_l are the chemical potential of the gaseous and liquid PFH, respectively. The fate of a nucleus depends on its radius r compared to the critical radius r^* for which the nucleus has equal chance to grow or to shrink (with $\mu_g = \mu_l$)[19]

$$r^* = \frac{2\gamma_{gl}(r^*)}{P_v - P_l^*} \quad (17)$$

where P_v and P_l^* are the vapor pressure of PFH and the critical pressure leading to the nucleus appearance, respectively. The nucleation energy $W^{hom}(r)$ required to obtain a nucleus of critical radius $r = r^*$ is then

$$W^{hom}(r^*) = \frac{16\pi\gamma_{gl}^3(r^*)}{3(P_v - P_l^*)^2} \quad (18)$$

Since at r^* the probability of the nucleus to grow is 1/2, the probability to obtain a vaporization of the droplet is also 1/2, thus $W^{hom}(r = r^*) = W^{hom}(q_{\geq 1} = 0.5)$. Taking into account the Laplace equation between the pressure inside and outside the droplet (respectively, P_l^* and $P_{0.5}^{(1)}$)

$$P_l^* = P_{0.5}^{(1)} + \frac{2\gamma_{lc}}{R} \quad (19)$$

After equalizing eq 18 and 15 and replacing $V = \frac{4}{3}\pi R^3$, we obtain

$$P_{0.5}^{(1)} = P_v - \sqrt{\frac{16\pi\gamma_{gl}^3(r^*)}{3k_B T \ln\left(\frac{2\pi J_0 R^3}{3f\ln(2)}\right)}} - \frac{2\gamma_{lc}}{R} \quad (20)$$

Since all parameters in eq 20 are known, this equation can be used to estimate the values $P_{0.5}^{(1)}$ for various droplet radii. On doing so, the equation predicts values of $|P_{0.5}^{(1)}|$ greater than 12 MPa irrespective of the droplet radius, which are much larger than our experimental values, as shown in Figure 9. In addition, the homogeneous nucleation model predicts a smaller variation of $P_{0.5}^{(1)}$ compared to the experimental values in the range of investigated droplet radius. The homogeneous model can also be applied to the case of water single-core and multicore PFH droplets by considering the total volume V of PFH inside the droplet in eq 15, thus excluding the water volume which cannot participate in the vaporization. By doing so, the model predicts the following: (i) the ADV pressure threshold should not change between water single-core and multicore PFH droplets as the volume of PFH is identical and

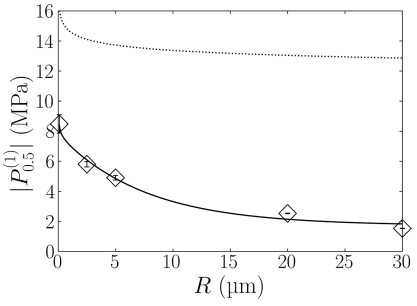

Figure 9. The diamonds are the values $|P_{0.5}^{(1)}|$ previously given in Figure 7. The dotted line represents the prediction of the homogeneous nucleation model. The solid line is the prediction given by the heterogeneous nucleation model, where γ_{gc} is the only unknown parameter, whose values are given in Figure 11B.

https://doi.org/10.1021/acs.langmuir.3c02272
Langmuir 2023, 39, 15716−15729

(ii) the threshold should diminish when the volume of PFH increases in water multicore PFH droplets. These two predictions are opposite to what was experimentally observed in Figure 8. In summary, the model of homogeneous nucleation fails to predict the results of all of our experiments, and consequently, it is not the mechanism responsible for ADV in our experimental conditions.

Development of a Model of Heterogeneous Nucleation and Comparison with Experimental Data. In heterogeneous nucleation, a nucleus appears at an interface present in the system. In the case of plain PFH droplet, it will be the single interface between PFH and glycerol. Similar to the homogeneous nucleation, the energy of heterogeneous nucleation is given by

$$W^{\mathrm{het}}(q_{\geq 1}) = k_{\mathrm{B}}T \ln\left(\frac{\Pi_0 A \tau}{\ln\left(\frac{1}{1-q_{\geq 1}}\right)}\right) \tag{21}$$

where Π_0 is the rate of heterogeneous nucleation[38] and A is the surface area of the interface on which the nucleus can appear. The work needed to create a nucleus is[38] (see Figure 10)

$$\begin{aligned} W^{het}(r_1, r_2) &= \gamma_{gl}(r_1)a(\psi, r_1) + \gamma_{gc}(r_2)a(\varphi, r_2) \\ &\quad - \gamma_{lc}a(\chi, R) \\ &\quad - (P_g - P_l)v + n_{\mathrm{PFH}}(\mu_g - \mu_l), \end{aligned} \tag{22}$$

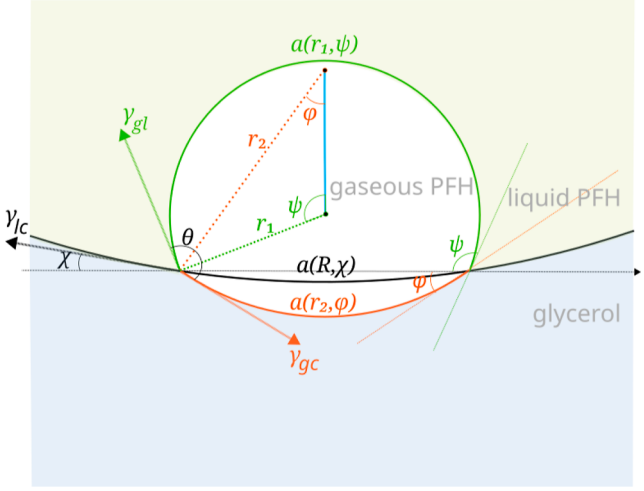

Figure 10. Schema of a nucleus on the surface of a plain PFH droplet surface (represented by the black solid line). The surface of the nucleus is represented by the green (with no surfactants) and orange (covered with surfactants) solid lines.

where $a(\psi, r_1)$ is the surface area of the gaseous PFH nucleus in contact with liquid PFH and $a(\varphi, r_2)$ is the surface area of the nucleus in contact with the surfactant droplet shell that was previously in contact with liquid PFH with a surface area $a(\chi, R)$. We have

$$a(\nu, r) = 2\pi r^2(1 - \cos\nu) \tag{23}$$

where $\nu = \psi, \varphi$, or χ, and $r = r_1, r_2$ or R. The nucleus volume is

$$v = \frac{\pi}{3}[r_1^3(2 - 3\cos\psi + \cos^3\psi) + r_2^3(2 - 3\cos\varphi + \cos^3\varphi)] \tag{24}$$

If the critical radii r_1^* and r_2^* are known, then the pressure $P_{0.5}^{(1)}$ could be predicted by solving the equation

$$W^{\mathrm{het}}(r_1^*, r_2^*) - W(q_{\geq 1} = 0.5) = 0 \tag{25}$$

Since the nucleus is at equilibrium at $r_1 = r_1^*$ and $r_2 = r_2^*$ (where we have $\mu_g = \mu_l$ and $P_g = P_v$), the Young−Laplace equations can be written for the three interfaces: liquid PFH/glycerol, gaseous PFH/liquid PFH, and gaseous PFH/glycerol

$$P_v = P_l^* + \frac{2\gamma_{gl}(r_1^*)}{r_1^*} \tag{26}$$

$$P_v = P_A^* + \frac{2\gamma_{gc}(r_2^*)}{r_2^*} \tag{27}$$

$$P_l^* = P_A^* + \frac{2\gamma_{lc}}{R} \tag{28}$$

We can easily determine the critical radii from these equations

$$r_1^* = \frac{2\gamma_{gl}(r_1^*)}{(P_v - P_l^*)} \tag{29}$$

$$r_2^* = \frac{2\gamma_{gc}(r_2^*)}{(P_v - P_l^*) + \frac{2\gamma_{lc}}{R}} \tag{30}$$

The calculation of the surface area and volume of the nucleus depend on the critical angles χ^*, ψ^*, and φ^* (see Figure 10). All the cosine of these angles can be written as a function on the cosine of the angle $\theta^* = \psi^* + \varphi^*$ (see Supporting Information)

$$\cos\varphi^* = \frac{r_2 + r_1\cos\theta^*}{\sqrt{r_1^* + r_2^* + 2r_1^*r_2^*\cos\theta^*}} \tag{31}$$

$$\cos\psi^* = \frac{r_2^*\cos\theta^* + r_1^*}{\sqrt{r_1^* + r_2^* + 2r_1^*r_2^*\cos\theta^*}} \tag{32}$$

$$\cos\chi^* = \sqrt{1 - \left(\frac{r_2^*}{R}\right)^2\left(1 - \left(\frac{r_2^* + r_1^*\cos\theta^*}{\sqrt{r_1^* + r_2^* + 2r_1^*r_2^*\cos\theta^*}}\right)^2\right)} \tag{33}$$

In addition, the interfacial tensions should verify the equation (see Figure 10)

$$\gamma_{gl}(r_1^*)\cos\psi^* - \gamma_{lc}\cos\chi^* + \gamma_{gc}(r_2^*)\cos\varphi^* = 0 \tag{34}$$

It can be used to determine the value of $\cos\theta^*$ as it can be written as a second-degree equation $a\cos^2\theta^* + b\cos\theta^* + c = 0$, where

$$a = \gamma_{gl}^2(r_1^*)r_2^{*2} + \gamma_{gc}^2(r_2^*)r_1^{*2} - \frac{\gamma_{lc}^2 r_1^{*2} r_2^{*2}}{R^2} + 2\gamma_{gl}(r_1^*)\gamma_{gc}(r_2^*)r_1^*r_2^* \tag{35}$$

https://doi.org/10.1021/acs.langmuir.3c02272
Langmuir 2023, 39, 15716−15729

$$b = 2(\gamma_{gl}^2(r_1^*) + \gamma_{gc}^2(r_2^*) - \gamma_{lc}^2)r_1^* r_2^* + 2\gamma_{gl}(r_1^*)\gamma_{gc}(r_2^*)(r_1^{*2} + r_2^{*2}) \quad (36)$$

$$c = (\gamma_{gl}^2(r_1^*) - \gamma_{lc}^2)r_1^{*2} + (\gamma_{gc}^2(r_2^*) - \gamma_{lc}^2)r_2^{*2} + 2\gamma_{gl}(r_1^*)\gamma_{gc}(r_2^*)r_1^* r_2^* + \frac{\gamma_{lc}^2 r_1^{*2} r_2^{*2}}{R^2} \quad (37)$$

$\cos\theta^*$ is thus simply

$$\cos\theta^* = \frac{-b \pm \sqrt{b^2 - 4ac}}{2a} \quad (38)$$

The value $W^{het}(r_1^*, r_2^*)$ can be calculated numerically using the values r_1^*, r_2^*, and $\cos\theta^*$, knowing that at equilibrium, $\mu_g = \mu_l$ and $P_g^* = P_v$.

However, in the presence of a surfactant, an interfacial tension strongly depends on the surface concentration of the surfactant. The appearance of a nucleus at the interface glycerol/PFC should lead to a local increase in the surface area of the interface and hence to a decrease in surfactant surface concentration. A variation in the value of $\gamma_{gc}(r_2^*)$ is then expected. No change in the values of $\gamma_{lc}(R)$ and $\gamma_{gl}(R)$ are expected since, respectively, the droplet radius R did not change and no surfactant was located at the interface between gaseous and liquid PFH. Consequently, we numerically solved eq 25 by considering $\gamma_{gc}(r_2^*)$ as an unknown parameter and using the experimental values $P_{0.5}^{(1)}$ (from Figure 7). By doing so, eq 25 can be numerically solved only if γ_{gc} decreases as the nucleus radius r_2^* increases as displayed in Figure 11A. The values r_1^* and r_2^* are plotted in Figure 12 to provide the shape of the nucleus for the various plain PFH droplet radii. We

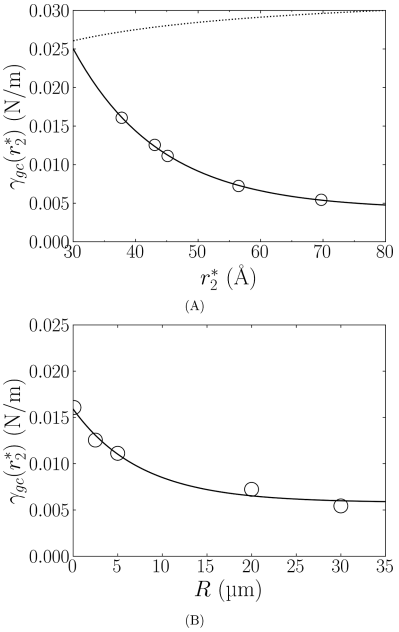

Figure 11. (A) The circles are the interfacial tension of the interface (of curvature $1/r_2^*$) between gaseous PFH and water $\gamma_{gc}(r_2^*)$ obtained as a solution of the eq 25 with δ = 4 Å. The dotted line represents what should be the variation of $\gamma_{gc}(r_2^*)$ if only a Tolman correction was applied to the experimental value γ_{gc} = 0.033 N/m. (B) Same values as previously but as a function of the droplet radius R. The solid lines in both figures are fits by a decreasing exponential.

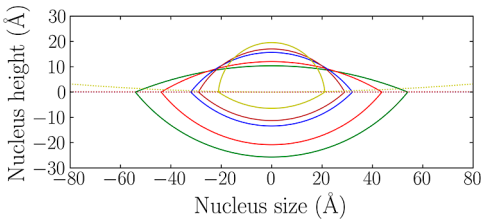

Figure 12. Figure displays the shape of the nucleus having radii r_1^* and r_2^* as showed by the solid lines. The dotted lines show the curvature of the droplet with radius R, where the liquid PFH is located on the top part of the graph. The nucleus size changes with the droplet radius R, where the colors green, red, blue, brown, and yellow are for R = 30, 20, 5, 2.5, and 0.1 μm, respectively.

observe that both radii decrease as R decreases, while the value $|P_l^*|$ increases (see Figure 11B). The nucleus volume is equal to v = 22, 41, 50, 104, and 175 nm^3 when the droplet radius is, respectively, equal to R = 0.1, 2.5, 5, 20, and 30 μm. Note that we used a Tolman length equal to 4 Å.[40] The system could not be solved using a larger value. Smaller values of δ only lead to smaller variation in nucleus size and $\gamma_{gl}(r_2^*)$.

We use the fit of $\gamma_{gl}(r_2^*)$ values as a function of R (given in Figure 11B) to predict the values of $P_{0.5}^{(1)}$ by numerically solving eq 25. The predicted values are given in Figure 9 as a solid line, and it shows that the model of heterogeneous nucleation is able to predict the correct behavior of $P_{0.5}^{(n)}$ as a function of the radius of plain PFH droplets. The prediction line is identical irrespective of the choice of δ as it will be balanced by a change in the γ_{gc} values. The question of understanding the behavior of $\gamma_{gc}(r_2^*)$ remains. It cannot be the result of a curvature effect as given by the Tolman equation (dotted line in Figure 11A) or of a decrease in surfactant surface concentration, since an increase in $\gamma_{gc}(r_2^*)$ would have been expected. But it can be explained if some PFH molecules, close to the droplet surface, are getting embedded into the surfactant layer during the formation of a gaseous PFH nucleus. This insertion leads to a decrease in the interfacial tension $\gamma_{gc}(r_2^*)$ as the surface area is more covered. The insertion is possible if there is enough room for the surfactant layer to accommodate PFH molecules. The available space is decreasing as the curvature (i.e., $1/r_2^*$) is increasing; indeed in such a case, the surfactant fluorocarbon chains are getting compact. Consequently, the lower the curvature, the larger the number of PFH molecules that can be inserted into the surfactant layer and smaller the value of $\gamma_{gc}(r_2^*)$

The heterogeneous model can also be applied to the case of water single-core and multicore droplets. In this case, the nucleation can take place either at the surface of the interface in contact with glycerol, as previously, or at the surface of the encapsulated water droplet(s). Similarly to plain PFH droplets, a model of heterogeneous nucleation can be written for the PFH/water interface of the encapsulated water by replacing R by the water droplet radius R_w (with a change of sign in one of the Young−Laplace equations) and using the values γ_{lw} and γ_{gw} in the presence of Krytox (see Table 2)) instead of γ_{lc} and γ_{gc}. The parameters leading to the occurrence of nucleation preferentially on one interface rather than the other one are mainly the droplet radius, the droplet surface area, and the interfacial tensions.

The experimental data displayed in Figure 8 show no change in the values of ADV threshold as the number of encapsulated water droplets increases in water multicore PFH droplets. In

https://doi.org/10.1021/acs.langmuir.3c02272
Langmuir 2023, 39, 15716−15729

addition, these values are similar to the value measured for a droplet devoid of water droplets (i.e., plain PFH droplets). If the nucleation would have occurred at the water/PFH interface of water droplets, a decrease in ADV threshold would have been expected because the total surface area of the interface water/PDH has increased (due to the increase in the number of water droplets) since it would lead to a higher probability of nucleation according to eq 21. We conclude that nucleation is preferentially occurring on the surface of the PFH/glycerol interface at a mean ADV pressure threshold of $|\left\langle P_{0.5}^{(1)} \right\rangle| = 2.8 \pm 0.1$ MPa. This value is characteristic of the properties of the PFH/glycerol interfaces (i.e., radius, surface area, and interfacial tensions), which are identical between all the droplet types.

For a droplet encapsulating a micron-sized droplet, the value of ADV threshold is $|P_{0.5}^{(1)}| = 1.9 \pm 0.1$ MPa, thus smaller than 2.8 ± 0.1 MPa. This suggests that nucleation is preferentially occurring at the surface of the PFH/water interface of the encapsulated water droplet rather than the PFH/glycerol interface.

The difference observed between water single-core and multicore PFH droplets comes from the difference in the water droplet radius. Indeed, our model indicates that the energy required to form a gas nucleus at a surface of micron-sized water droplet is lower than at a surface exhibiting a larger curvature. Our results also suggest that the energy required to form a nucleus at the water/PFH interface of nanometric-sized water droplets is larger than that at the PFH/glycerol interface (of the micron-size droplet encapsulating the water droplets). In this case, the difference arises not only due to a difference in surface curvature but also because the surfactants (hence the respective interfacial tensions) are different between the two interfaces.

CONCLUSIONS

The acoustic vaporization pressure threshold $P_{0.5}^{(n)}$ strongly depends on the number of insonified droplets. We showed that the threshold value for only one insonified droplet, $P_{0.5}^{(1)}$, can be obtained either by diluting the droplet solution or by using a statistical model, which can derive this value from the probability curves measured on droplet solution.

When considering plain PFH droplets, the $P_{0.5}^{(1)}$ value decreases as the radius of the plain PFH droplets increases. The threshold $P_{0.5}^{(1)}$ can be reduced by encapsulating a micron-sized water droplet. However, the encapsulation of many nanometer-sized water droplets induces no modification in the $P_{0.5}^{(1)}$ value.

Our experimental conditions prevent the occurrence of superharmonic focusing. The experimental data performed on plain PFH droplets and water single-core and multicore PFH droplets cannot be explained by homogeneous nucleation, and the model of homogeneous nucleation fails to predict the data of plain PFH droplets. However, all experimental results can be explained by heterogeneous nucleation, where the nucleation occurs either on the PFH/glycerol surface of the droplet or on the PFH/water surface of the encapsulated water droplets. We derived equations modeling heterogeneous nucleation that were successful to describe the behavior of $P_{0.5}^{(1)}$ as a function of the radius of a plain PFH droplet. The model uses three parameters: interfacial tensions, the droplet radii, and the vapor pressure of the perfluorocarbon. Thus, the model can be used for any kind of perfluorocarbons and any temperature as long as the values of these parameters are known.

ASSOCIATED CONTENT

Supporting Information

The Supporting Information is available free of charge at https://pubs.acs.org/doi/10.1021/acs.langmuir.3c02272.

Detailed derivations of equations used in the manuscript; size distribution of water single-core droplets, light scattering measurement on nanometric-sized PFH droplets, acoustic signal of samples, curves showing the absence of superharmonic focusing, schema with notation used in the previous equations; and short bibliography (PDF)

AUTHOR INFORMATION

Corresponding Author

N. Taulier − *CNRS, INSERM, Laboratoire d'Imagerie Biomédicale, LIB, Sorbonne Université, F-75006 Paris, France;* orcid.org/0000-0003-1017-1068; Email: nicolas.taulier@cnrs.fr

Authors

R. Ramesh − *CNRS, INSERM, Laboratoire d'Imagerie Biomédicale, LIB, Sorbonne Université, F-75006 Paris, France; Laboratoire de Physique de l'École Normale Supérieure, ENS, Université PSL, CNRS, Sorbonne Université, Université de Paris Cité, F-75005 Paris, France*

C. Thimonier − *CNRS, INSERM, Laboratoire d'Imagerie Biomédicale, LIB, Sorbonne Université, F-75006 Paris, France; Laboratoire de Physique de l'École Normale Supérieure, ENS, Université PSL, CNRS, Sorbonne Université, Université de Paris Cité, F-75005 Paris, France; Département de Chimie, P.A.S.T.E.U.R., École Normale Supérieure, Université PSL, Sorbonne Université, CNRS, 75005 Paris, France*

S. Desgranges − *Équipe Systèmes Amphiphiles Bioactifs et Formulations Eco-compatibles, UPRI, Avignon Université, 84000 Avignon, France*

V. Faugeras − *Laboratoire de Physique de l'École Normale Supérieure, ENS, Université PSL, CNRS, Sorbonne Université, Université de Paris Cité, F-75005 Paris, France*

F. Coulouvrat − *Institut Jean le Rond d'Alembert, CNRS, Sorbonne Université, 75005 Paris, France*

J. Laurent − *Laboratoire de Physique et Mécanique des Milieux Hétérogènes, CNRS, ESPCI Paris, PSL Research University, Sorbonne Université, Université Paris Cité, 75005 Paris, France*

G. Marrelec − *CNRS, INSERM, Laboratoire d'Imagerie Biomédicale, LIB, Sorbonne Université, F-75006 Paris, France*

C. Contino-Pépin − *Équipe Systèmes Amphiphiles Bioactifs et Formulations Eco-compatibles, UPRI, Avignon Université, 84000 Avignon, France;* orcid.org/0000-0002-0125-5342

W. Urbach − *Laboratoire de Physique de l'École Normale Supérieure, ENS, Université PSL, CNRS, Sorbonne Université, Université Paris Cité, F-75005 Paris, France;* orcid.org/0000-0002-1673-6923

C. Tribet − *PASTEUR, Département de Chimie, École Normale Supérieure, PSL University, Sorbonne Université,*

https://doi.org/10.1021/acs.langmuir.3c02272
Langmuir 2023, 39, 15716−15729

CNRS, 75005 Paris, France; orcid.org/0000-0002-5953-0968

Complete contact information is available at: https://pubs.acs.org/10.1021/acs.langmuir.3c02272

Author Contributions

○R.R. and C.T. contributed equally.

Notes

The authors declare no competing financial interest.

■ ACKNOWLEDGMENTS

The authors acknowledge the funding from Plan cancer 2014-2019 (Project BubDrop4Glio). The Ph.D scholarship of C.T. was funded by ITMO cancer.

■ REFERENCES

(1) Crouse, L. J.; Cheirif, J.; Hanly, D. E.; Kisslo, J. A.; Labovitz, A. J.; Raichlen, J. S.; Schutz, R. W.; Shah, P. M.; Smith, M. D. Opacification and border delineation improvement in patients with suboptimal endocardial border definition in routine echocardiography: Results of the phase III Albunex multicenter trial. *J. Am. Coll. Cardiol.* **1993**, *22*, 1494−1500.

(2) Harmon, J. N.; Kabinejadian, F.; Seda, R.; Fabiilli, M. L.; Kuruvilla, S.; Kuo, C. C.; Greve, J. M.; Fowlkes, J. B.; Bull, J. L. Minimally invasive gas embolization using acoustic droplet vaporization in a rodent model of hepatocellular carcinoma. *Sci. Rep.* **2019**, *9*, 11040.

(3) Fabiilli, M. L.; Haworth, K. J.; Fakhri, N. H.; Kripfgans, O. D.; Carson, P. L.; Fowlkes, J. B. The role of inertial cavitation in acoustic droplet vaporization. *IEEE Trans. Ultrason. Eng.* **2009**, *56*, 1006−1017.

(4) Aliabouzar, M.; Kumar, K. N.; Sarkar, K. Effects of droplet size and perfluorocarbon boiling point on the frequency dependence of acoustic vaporization threshold. *J. Acoust. Soc. Am.* **2019**, *145*, 1105−1116.

(5) Kripfgans, O. D.; Fowlkes, J. B.; Woydt, M.; Eldevik, O. P.; Carson, P. L. In vivo droplet vaporization for occlusion therapy and phase aberration correction. *IEEE Trans. Ultrason. Eng.* **2002**, *49*, 726−738.

(6) Sokka, S. D.; King, R.; Hynynen, K. MRI-guided gas bubble enhanced ultrasound heating in in vivo rabbit thigh. *Phys. Med. Biol.* **2003**, *48*, 223−241.

(7) Zhang, P.; Porter, T. An in vitro Study of a Phase-Shift Nanoemulsion: A Potential Nucleation Agent for Bubble-Enhanced HIFU Tumor Ablation. *Ultrasound Med. Biol.* **2010**, *36*, 1856−1866.

(8) Zhang, M.; Fabiilli, M. L.; Haworth, K. J.; Padilla, F.; Swanson, S. D.; Kripfgans, O. D.; Carson, P. L.; Fowlkes, J. B. Acoustic Droplet Vaporization for Enhancement of Thermal Ablation by High Intensity Focused Ultrasound. *Acad. Radiol.* **2011**, *18*, 1123−1132.

(9) Chen, C. C.; Sheeran, P. S.; Wu, S.-Y.; Olumolade, O. O.; Dayton, P. A.; Konofagou, E. E. Targeted drug delivery with focused ultrasound-induced blood-brain barrier opening using acoustically-activated nanodroplets. *J. Control* **2013**, *172*, 795−804.

(10) Giesecke, T.; Hynynen, K. Ultrasound-mediated cavitation thresholds of liquid perfluorocarbon droplets in vitro. *Ultrasound Med. Biol.* **2003**, *29*, 1359−1365.

(11) Schad, K. C.; Hynynen, K. In vitro characterization of perfluorocarbon droplets for focused ultrasound therapy. *Phys. Med. Biol.* **2010**, *55*, 4933−4947.

(12) Williams, R.; Wright, C.; Cherin, E.; Reznik, N.; Lee, M.; Gorelikov, I.; Foster, F. S.; Matsuura, N.; Burns, P. N. Characterization of Submicron Phase-change Perfluorocarbon Droplets for Extravascular Ultrasound Imaging of Cancer. *Ultrasound Med. Biol.* **2013**, *39*, 475−489.

(13) Martz, T. D.; Sheeran, P. S.; Bardin, D.; Lee, A. P.; Dayton, P. A. Precision Manufacture of Phase-Change Perfluorocarbon Droplets Using Microfluidics. *Ultrasound Med. Biol.* **2011**, *37*, 1952−1957.

(14) Sheeran, P. S.; Luois, S. H.; Mullin, L. B.; Matsunaga, T. O.; Dayton, P. A. Design of ultrasonically-activatable nanoparticles using low boiling point perfluorocarbons. *Biomaterials* **2012**, *33*, 3262−3269.

(15) Shpak, O.; Kokhuis, T. J. A.; Luan, Y.; Lohse, D.; de Jong, N.; Fowlkes, B.; Fabiilli, M.; Versluis, M. Ultrafast dynamics of the acoustic vaporization of phase-change microdroplets. *J. Acoust. Soc. Am.* **2013**, *134*, 1610−1621.

(16) Kripfgans, O. D.; Fowlkes, J. B.; Miller, D. L.; Eldevik, O. P.; Carson, P. L. Acoustic droplet vaporization for therapeutic and diagnostic applications. *Ultrasound Med. Biol.* **2000**, *26*, 1177−1189.

(17) Sheeran, P. S.; Matsunaga, T. O.; Dayton, P. A. Phase change events of volatile liquid perfluorocarbon contrast agents produce unique acoustic signatures. *Phys. Med. Biol.* **2014**, *59*, 379−401.

(18) Lacour, T.; Valier-Brasier, T.; Coulouvrat, F. Ultimate fate of a dynamical bubble/droplet system following acoustic vaporization. *Phys. Fluids* **2020**, *32*, 051702.

(19) Fletcher, N. H. Size Effect in Heterogeneous Nucleation. *J. Chem. Phys.* **1958**, *29*, 572−576.

(20) Chattaraj, R.; Goldscheitter, G. M.; Yildirim, A.; Goodwin, A. P. Phase behavior of mixed lipid monolayers on perfluorocarbon nanoemulsions and its effect on acoustic contrast. *RSC Adv.* **2016**, *6*, 111318−111325.

(21) Shakya, G.; Hoff, S. E.; Wang, S.; Heinz, H.; Ding, X.; Borden, M. A. Vaporizable endoskeletal droplets via tunable interfacial melting transitions. *Sci. Adv.* **2020**, *6*, No. eaaz7188.

(22) Desgranges, S.; Lorton, O.; Gui-Levy, L.; Guillemin, P.; Celicanin, Z.; Hyacinthe, J.-N.; Breguet, R.; Crowe, L. A.; Becker, C. D.; Soulié, M.; Taulier, N.; Contino-Pépin, C.; Salomir, R. Micron-sized PFOB liquid core droplets stabilized with tailored-made perfluorinated surfactants as a new class of endovascular sonosensitizers for focused ultrasound thermotherapy. *J. Mater. Chem. B* **2019**, *7*, 927−939.

(23) Bodin-Thomazo, N.; Malloggi, F.; Guenoun, P. Marker patterning: a spatially resolved method for tuning the wettability of PDMS. *RSC Adv.* **2017**, *7*, 46514−46519.

(24) Mailer, A. G.; Clegg, P. S.; Pusey, P. N. Particle sizing by dynamic light scattering: non-linear cumulant analysis. *J. Phys.: Condens. Matter* **2015**, *27*, 145102.

(25) Morris, P.; Hurrell, A.; Shaw, A.; Zhang, E.; Beard, P. A Fabry−Pérot fiber-optic ultrasonic hydrophone for the simultaneous measurement of temperature and acoustic pressure. *J. Acoust. Soc. Am.* **2009**, *125*, 3611−3622.

(26) Holland, C. K.; Apfel, R. E. Thresholds for transient cavitation produced by pulsed ultrasound in a controlled nuclei environment. *J. Acoust. Soc. Am.* **1990**, *88*, 2059−2069.

(27) Apfel, R. E. Activatable infusable dispersions containing drops of a superheated liquid for methods of therapy and diagnosis. U.S. Patent 5,840,276 A, 1997.

(28) Johnston, K.; Tapia-Siles, C.; Gerold, B.; Postema, M.; Cochran, S.; Cuschieri, A.; Prentice, P. Periodic shock-emission from acoustically driven cavitation clouds: A source of the subharmonic signal. *Ultrasonics* **2014**, *54*, 2151−2158.

(29) Muir, T. G.; Carstensen, E. L. Prediction of nonlinear acoustic effects at biomedical frequencies and intensities. *Ultrasound Med. Biol.* **1980**, *6*, 345−357.

(30) Maxwell, A. D.; Cain, C. A.; Hall, T. L.; Fowlkes, J. B.; Xu, Z. Probability of Cavitation for Single Ultrasound Pulses Applied to Tissues and Tissue-Mimicking Materials. *Ultrasound Med. Biol.* **2013**, *39*, 449−465.

(31) Aliabouzar, M.; Lu, X.; Kripfgans, O. D.; Fowlkes, J. B.; Fabiilli, M. L. Acoustic Droplet Vaporization in Acoustically Responsive Scaffolds: Effects of Frequency of Excitation, Volume Fraction and Threshold Determination Method. *Ultrasound Med. Biol.* **2019**, *45*, 3246−3260.

(32) Radhakrishnan, K.; Bader, K. B.; Haworth, K. J.; Kopechek, J. A.; Raymond, J. L.; Huang, S.-L.; McPherson, D. D.; Holland, C. K. Relationship between cavitation and loss of echogenicity from ultrasound contrast agents. *Phys. Med. Biol.* **2013**, *58*, 6541−6563.

(33) Luís, A.; Shimizu, K.; Araújo, J. M.; Carvalho, P. J.; da Silva, J. A. L.; Lopes, J. N. C.; Rebelo, L. P.; Coutinho, J. A.; Freire, M. G.; Pereiro, A. B. Influence of Nanosegregation on the Surface Tension of Fluorinated Ionic Liquids. *Langmuir* **2016**, *32*, 6130−6139.
(34) Tolman, R. C. The Effect of Droplet Size on Surface Tension. *J. Chem. Phys.* **1949**, *17*, 333−337.
(35) Holten, V.; Labetski, D. G.; van Dongen, M. E. H. Homogeneous nucleation of water between 200 and 240 K: New wave tube data and estimation of the Tolman length. *J. Chem. Phys.* **2005**, *123*, 104505.
(36) Shpak, O.; Verweij, M.; Vos, H. J.; de Jong, N.; Lohse, D.; Versluis, M. Acoustic droplet vaporization is initiated by superharmonic focusing. *Proc. Nat. Acad. Sci.* **2014**, *111*, 1697−1702.
(37) Yuldashev, P. V.; Karzova, M. M.; Kreider, W.; Rosnitskiy, P. B.; Sapozhnikov, O. A.; Khokhlova, V. A. HIFU Beam:" A Simulator for Predicting Axially Symmetric Nonlinear Acoustic Fields Generated by Focused Transducers in a Layered Medium. *IEEE Trans. Ultrason. Eng.* **2021**, *68*, 2837−2852.
(38) Blander, M.; Katz, J. L. Bubble nucleation in liquids. *AIChE J.* **1975**, *21*, 833−848.
(39) Katz, J. L.; Blander, M. Condensation and boiling: Corrections to homogeneous nucleation theory for nonideal gases. *J. Colloid Interface Sci.* **1973**, *42*, 496−502.
(40) de Aguiar, H. B.; de Beer, A. G. F.; Strader, M. L.; Roke, S. The Interfacial Tension of Nanoscopic Oil Droplets in Water Is Hardly Affected by SDS Surfactant. *J. Am. Chem. Soc.* **2010**, *132*, 2122−2123.

https://doi.org/10.1021/acs.langmuir.3c02272
Langmuir 2023, 39, 15716−15729